PAPER

3D honeycombed cobalt, nitrogen co-doped carbon nanosheets via hypersaline-protected pyrolysis towards efficient oxygen reduction

IOP Publishing Nanotechnology

Nanotechnology **31** (2020) 364003 (8pp) https://doi.org/10.1088/1361-6528/ab97d5

3D honeycombed cobalt, nitrogen co-doped carbon nanosheets via hypersaline-protected pyrolysis towards efficient oxygen reduction

Yong Zheng[1,4], Shan Chen[1,4], Hengyi Lu[1], Chao Zhang[1] and Tianxi Liu[1,2,3]

[1] State Key Laboratory for Modification of Chemical Fibers and Polymer Materials, College of Materials Science and Engineering, Innovation Center for Textile Science and Technology, Donghua University, Shanghai 201620, People's Republic of China
[2] Key Laboratory of Synthetic and Biological Colloids, Ministry of Education, School of Chemical and Material Engineering, Jiangnan University, Wuxi 214122, People's Republic of China
[3] Key Laboratory of Materials Processing and Mold (Zhengzhou University), Ministry of Education, Zhengzhou 450002, People's Republic of China

E-mail: czhang@dhu.edu.cn and txliu@fudan.edu.cn

Received 21 April 2020, revised 17 May 2020
Accepted for publication 29 May 2020
Published 22 June 2020

Abstract

The broad application of metal-air batteries and fuel cells have been greatly limited due to their slow kinetics of oxygen electrodes involving the oxygen reduction reaction (ORR), and therefore the development of high-efficient, low-cost and high-reserve ORR electrocatalysts is of great significance. Herein, a hypersaline-protected pyrolysis strategy is presented for preparing 3D honeycombed cobalt, nitrogen co-doped carbon nanosheets (Co/N-CNS) by using eco-friendly biomass as a carbon and nitrogen source. During the hypersaline-protected pyrolysis, the pyridinic nitrogen-rich biomass facilitates the formation of highly active Co/N active sites among the resultant Co/N-CNS, while the templating-washing-drying cyclic utilization of salts creates honeycombed pore structures among the Co/N-CNS. Due to the structural features of honeycombed pores and uniform distributed active sites, the Co/N-CNS catalyst offers excellent ORR activity, high durability and methanol-tolerant performance in an alkaline electrolyte. As a demonstration, a primary Zn-air battery using the Co/N-CNS cathode delivers a high power density and excellent operating stability beyond that of commercial Pt/C cathode.

Supplementary material for this article is available online

Keywords: hypersaline-protected pyrolysis, honeycombed carbon nanosheets, cobalt and nitrogen co-doping, oxygen reduction reaction, Zn-air battery

(Some figures may appear in colour only in the online journal)

1. Introduction

Metal-air batteries and fuel cells have been broadly developed in recent years due to their high energy conversion efficiency, environmentally benign nature and safety in operation [1–5]. The slow kinetics of cathodic oxygen reduction reaction (ORR) in the oxygen electrodes is a rate-determining step limiting their large-scale applications [6]. Precious metal-free ORR catalysts are attracting broad attention due to their low prices, rich reserves, strong anti-poisoning ability

[4] Y.Z. and S.C. contributed equally to this work.

and long cycling stability, when compared with commercial Pt/C catalyst. Among them, nitrogen-doped (N-doped) carbon with the low-cost, highly active and durable features has shown great potentials substituting to commercial Pt/C catalyst [7–10]. Recently, a variety of eco-friendly and low-cost biomass is widely used for the preparation of N-doped carbon [11, 12]. However, there are great challenges in the direct pyrolysis of biomasses into N-doped carbon due to severe losses of nitrogen components, low carbonization yields and low porosities of products.

Simultaneous doping of transition metals (Co, Fe, Ni, Mn, etc) into N-doped carbon usually possesses greatly enhanced ORR performance far beyond N-doped carbon [2, 13–16]. The utilization of carbon- and nitrogen-containing precursors are often concerned for pyrolysis preparation of transition metal/nitrogen co-doped carbon [17–20]. However, the simple pyrolysis of carbon, nitrogen and transition metal-containing precursors usually produces the co-doped carbon with low specific surface area, unsatisfying porosity and inadequate exposure of active sites [21]. The introduction of a hierarchically porous structure into doped carbon materials can well solve these problems by increasing exposed active sites and accelerating ion/electron/oxygen transferring during subsequent ORR processes [22–25]. So far, hard- and soft-templating methods have been widely used to create pore structures among the pyrolyzed carbon, however, these templating methods are greatly limited due to the uses of complex operation process, toxic reagents and highly expensive templates [26, 27]. Therefore, there are great challenges for developing hierarchically porous doped carbon in a simple, effective and environmental-friendly way.

Herein, a hypersaline-protected pyrolysis strategy is presented for the synthesis of cobalt, nitrogen co-doped carbon nanosheets (Co/N-CNS). During the hypersaline-protected pyrolysis, the Co/N-CNS with honeycombed pore structure is generated due to templating-washing-drying cyclic utilization of NaCl salts, while an eco-friendly biomass vitamin B2 (VB2) is used as a carbon and nitrogen source. Due to unique structural features of honeycombed porosity and uniformly distributed active sites, the Co/N-CNS catalyst with high electron/ion/oxygen transports delivers high ORR catalytic activity and excellent cycling/methanol-tolerant stability. As a demonstration, as-assembled Zn-air battery using the Co/N-CNS cathode displays high power density and excellent operating stability, demonstrating its great potential to replace commercial Pt/C cathode in the practical applications.

2. Experimental details

2.1. Preparation of the Co/N-CNS

Typically, 1 g of VB2 was dissolved in 20 ml of aqueous solution containing designed amounts of NaCl and $Co(OAc)_2{\cdot}4H_2O$. Upon lyophilization, the power mixture was pyrolyzed at 800 °C with a heating rate of 5 °C min^{-1} under a nitrogen flow, washed with 1 M HCl and water, and then dried in vacuum at 60 °C overnight. The Co/N-CNS-0, Co/N-CNS-1 and Co/N-CNS-2 represent the products obtained with NaCl/VB2 mass ratio of 0, 3 and 6, respectively, keeping VB2/$Co(OAc)_2$ mass ratio of 20. The Co/N-CNS-2(Co1) and Co/N-CNS-2(Co3) represent the products with VB2/$Co(OAc)_2$ mass ratio of 40 and 10, respectively, with other pyrolysis conditions similar with that of Co/N-CNS-2. Pyrolysis temperature T was tailored at 700 °C and 900 °C, respectively, and the products were denoted as the Co/N-CNS-2(T), with other pyrolysis condition similar with that of Co/N-CNS-2.

2.2. Preparation of the Co/N-C and N-CNS

The Co/N-C was prepared by direct pyrolysis of grinded mixture of NaCl, VB2 and $Co(OAc)_2{\cdot}4H_2O$, with other pyrolysis condition similar with that of Co/N-CNS-2. The N-CNS was prepared without the addition of $Co(OAc)_2{\cdot}4H_2O$, with other pyrolysis condition similar with that of Co/N-CNS-2.

3. Result and discussion

Figure 1 demonstrates the hypersaline-protected pyrolysis procedures for the preparation of the Co/N-CNS. First, the VB2 and $Co(OAc)_2{\cdot}4H_2O$ were fully dissolved in saturated NaCl solution, which was then lyophilized into a powder mixture. Second, the powder mixture was pyrolyzed in a nitrogen flow, then washed with 1 M HCl and water, and dried at 80 °C in vacuum, thus to obtain the Co/N-CNS. The hypersaline-protected pyrolysis strategy facilitates an intriguing batch production of the honeycombed carbon structures with templating-washing-drying cyclic reutilization of NaCl salts. Namely, during the hypersaline-protected pyrolysis, NaCl salts act as initial reactants, templates and final by-products for the formation of the Co/N-CNS. By simply enlarging the use of initial reactants with the same proportion, 20 g of Co/N-CNS can be one-batch prepared. Biomass VB2 with abundant pyridinic nitrogen-rich structure, low cost and eco-friendly property acts as carbon and nitrogen sources during the hypersaline-protected pyrolysis. Besides, multi-hydroxyl polysaccharide structure in VB2 facilitates high carbonization yield, while abundant polar oxygen-containing groups (i.e. -OH, -CO-NH-) in VB2 show excellent compatibility with NaCl crystals before subsequent pyrolysis. Notably, biomass VB2 typically shows a substantially high solubility in saturated NaCl solution while other conventional biomasses always show a precipitating tendency in concentrated salt solution.

The structural evolution of honeycombed pore structures among the Co/N-CNS was investigated by varying different feeding ratios of NaCl salts. The Co/N-CNS-0 without the addition of NaCl templates shows a micron-sized irregular morphology with no obvious pore structures from the scanning electronic microscopy (SEM) observation (figure 2(a)). The Co/N-CNS-1 with addition of small amounts of NaCl templates shows morphology of assembled carbon nanosheets with micron-sized pores (figure 2(b)). The Co/N-CNS-2 with an increased feeding NaCl ratio shows morphology of 3D honeycombed network constructed with ultrathin carbon nanosheets (figure 2(c)). Pyrolysis temperature also

Figure 1. Schematic illustration of hypersaline-protected pyrolysis procedures of the Co/N-CNS by templating-washing-drying cyclic utilization of NaCl salts.

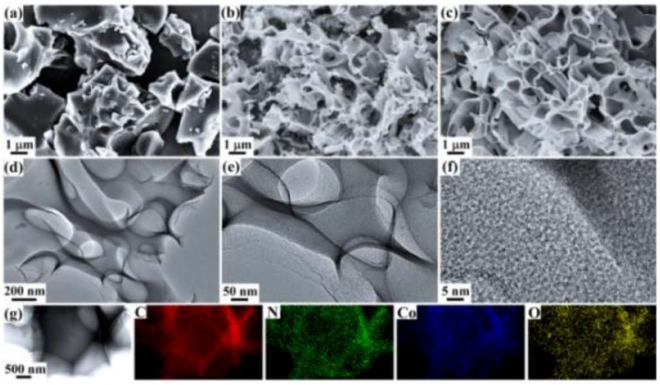

Figure 2. SEM images of (a) Co/N-CNS-0, (b) Co/N-CNS-1, (c) Co/N-CNS-2. (d, e) TEM and (f) HRTEM images of the Co/N-CNS-2. (g) Bright-field TEM image of the Co/N-CNS-2 and corresponding elemental mappings, indicating the uniform distribution of C, N, Co and O elements in the Co/N-CNS-2.

plays an important role in the formation of the Co/N-CNS [28]. When pyrolysis temperature is 700 °C that is below melting point of NaCl, the Co/N-CNS-2(700) shows a morphology of aggregated fragments (figure S1(a) available online at (stacks.iop.org/Nano/31/364003/mmedia)), which is due to the insufficiency of volume exclusion and confinement effect of NaCl crystals during the pyrolysis. When the pyrolysis temperature is 800 °C that is higher than melting point of NaCl, honeycombed pore structures among the Co/N-CNS are generated, indicating that molten NaCl is beneficial for the formation of honeycombed pore structures. When the pyrolysis temperature further increases to 900 °C, the Co/N-CNS-2(900) exhibits morphology of aggregated carbon nanosheets because excessive temperature for pyrolysis will cause pore structure collapse of the Co/N-CNS (figure S1(b)).

Transmission electron microscopy (TEM) images further reveal the honeycombed pore structures among the Co/N-CNS-2, and the pore sizes are in the range of 50–150 nm (figures 2(d)–(e)). High-resolution TEM (HRTEM) image shows that the Co/N-CNS-2 consists of assembled carbon nanosheets with sub-10-nm graphitic carbon domains (figure 2(f)). The graphitic carbon domains with a lattice fringe spacing of 0.34 nm clearly indicate a high graphitization degree of Co/N-CNS-2. In addition, bright-field TEM image and EDS mappings (figure 2(g)) imply that the cobalt and nitrogen elements are uniformly distributed throughout the framework of Co/N-CNS-2. Control sample of Co/N-C was prepared by direct pyrolysis of grinded mixture of NaCl, VB2 and cobalt salts. The Co/N-C shows a morphology of micron-sized segments (figure S2), indicating that the lyophilizing process is essential for the construction of uniformly distributed honeycombed pore structures.

The formation mechanism for honeycombed pore structures among the Co/N-CNS via hypersaline-protected pyrolysis process is explained in the following. During the hypersaline-protected pyrolysis process, the early-generated nano-droplets of molten NaCl will serve as a fluid template [29, 30]. resulting in the formation of 3D interpenetrating pore structures among the Co/N-CNS-2. Upon cooling, millimeter-sized NaCl beads can be observed on the surface of as-obtained block products (figure S3), and the formation of surface-rich NaCl beads indicate that molten NaCl indeed flow through honeycombed pore walls due to unique capillary effect during pyrolysis. Therefore, the developed hypersaline-protected pyrolysis strategy provides a simple and efficient way to produce unique honeycombed carbon materials.

Figure 3(a) exhibits x-ray photoelectron spectroscopy (XPS) spectrum of the Co/N-CNS-2, indicating that nitrogen content in the Co/N-CNS-2 significantly increases to 4.61 at%, compared with that of Co/N-CNS-0 (3.16 at%), matching well with the elemental analysis (table S1). The hypersaline-protected pyrolysis strategy can effectively utilize nitrogen species within the precursor to obtain high-content N-doping among the resultant carbon. The unique salt encapsulation effect of NaCl greatly alleviates substantial losses of nitrogen species during subsequent pyrolysis, thus realizing the formation of highly active Co/N and pyridinic-N active sites within the Co/N-CNS.

XPS survey spectrum in figure S4(a) clearly reveals that Co/N-CNS-2 is composed of carbon (89.4 at%), nitrogen (4.6 at%), oxygen (5.4 at%) and cobalt (0.6 at%). The N 1s XPS spectra of Co/N-CNS-2(700), Co/N-CNS-2 and Co/N-CNS-2(900) in figure 3(b) indicate that the nitrogen types among the three samples are pyridinic-N, pyrrolic-N, graphitic-N and N-O, respectively [31, 32]. High content of pyridinic-N among the Co/N-CNS-2 clearly indicates that pyridinic N-rich structure among VB2 precursor plays an important role for the regulation of nitrogen species in the Co/N-CNS products. The Co/N-CNS-2 shows high pyridinic-N content at optimized pyrolysis temperatures, and the pyridinic-N structure favors the formation of Co/N coordination sites among the Co/N-CNS products [33–35], which is critical for boosting ORR catalytic performance [36]. The Co 2p XPS spectrum indicates that there are three peaks at 795.3, 784.7 and 780.3 eV among the of Co/N-CNS-2 (figure 3(c)), which are attributed to Co $2p^{1/2}$, Co-N_x and Co $2p^{3/2}$, respectively [37]. The Co-Nx species among the Co/N-CNS-2 clearly suggest the high-efficient ORR catalytic activity [38]. Therefore, the N 1s and Co 2p XPS peaks clearly indicate

efficient co-doping of cobalt and nitrogen elements into the Co/N-CNS-2. The peaks in C 1s XPS spectrum of the Co/N-CNS-2 at 284.5, 285.6, 286.6 and 287.6 eV can be assigned to the C=C, C-C, C=N and O–C=O, respectively (figure S4(b)). The C=N species further confirm that the nitrogen elements are doped into the Co/N-CNS-2, which subsequently improve ORR catalytic activity with fast charge mobility [39–41].

Defect structures of the Co/N-CNS are investigated by Raman characterizations [42, 43]. The intensity ratio of D and G bands (I_D/I_G) decreases with increased contents of NaCl template (figure 3(d)), indicating that the addition of NaCl templates is beneficial for improving graphitization degrees of the Co/N-CNS products. This result is attributed to an unique encapsulated effect of molten salts during the pyrolysis [44]. With increased contents of cobalt salts, the I_D/I_G ratios decrease from 1.07 to 0.94 (figure 3(e)), indicating that cobalt ions enhance the graphitization degrees of the Co/N-CNS, thus contributing to improving the electrical conductivity. Higher pyrolysis temperature will create the Co/N-CNS-2 with more ordered graphitic carbon structures ranging from 700 °C to 900 °C (figure S5) [45]. Figures S6(a) and (b) show x-ray diffraction (XRD) patterns of the Co/N-CNS prepared with different feeding cobalt contents and pyrolysis temperatures, respectively. The broad XRD patterns centered at 25.9° and 44.0° correspond to graphitic (002) and (100) lattice planes, respectively, clearly showing that heteroatom-doping causes the Co/N-CNS with defect-rich structures [46].

Nitrogen adsorption/desorption measurements indicate pore characteristics of the Co/N-CNS products. The Co/N-CNS-2 exhibits simultaneously emerged micropores and mesopores due to the presence of type-IV isotherm with a type-H2 hysteretic loop (figure 3(f)) [47]. The specific surface areas of the Co/N-CNS increase remarkably with increased contents of NaCl templates (table S2). The Co/N-CNS-0 indicates a low surface area of 15.5 $m^2\ g^{-1}$, while the Co/N-CNS-2 exhibits a high surface area of 512.9 $m^2\ g^{-1}$, indicating that NaCl templates facilitate the formation of large-surface-area pore structures. The mean pore size of the Co/N-CNS-2 is centered at 3.2 nm performed by density functional theory (DFT) analysis (figure S7). The volatilization of gases during pyrolysis can introduce rich mesopores among the Co/N-CNS. The pore volume of the Co/N-CNS-2 (0.32 ml g^{-1}) is approximately 15 times larger than that of Co/N-CNS-0 (0.02 ml g^{-1}). Nitrogen adsorption/desorption isotherms of the Co/N-CNS at different pyrolysis temperatures are also analyzed. The specific surface areas of the Co/N-CNS-2(700) and Co/N-CNS-2(900) are 23.1 and 373.1 ml g^{-1}, respectively, indicating that the honeycombed pore structures are not generated at relatively low pyrolysis temperature, and honeycombed pore structures will inevitably collapse at relatively high pyrolysis temperature.

The Co/N-CNS with unique structural features of 3D honeycombed pore structures, uniformly distributed Co/N active sites and intrinsically high electrical conductivity is promising to demonstrate excellent ORR catalytic performance [48–50]. Cyclic voltammetry (CV) curve of the Co/N-CNS-2 exhibits an obvious reduction peak centered at 0.82 V vs. RHE in O_2-saturated 0.1 M KOH (figure 4(a)), implying that

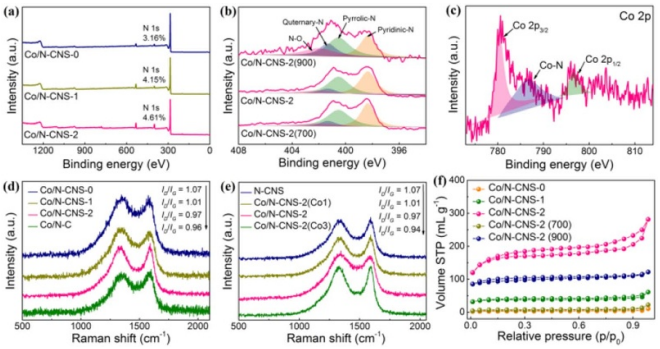

Figure 3. (a) XPS survey spectra of the Co/N-CNS-0, Co/N-CNS-1 and Co/N-CNS-2. (b) N 1s XPS spectra of the Co/N-CNS-2 prepared at different pyrolysis temperatures. (c) Co 2p XPS spectra of the Co/N-CNS-2. (d) Raman spectra of the Co/N-CNS-0, Co/N-CNS-1, Co/N-CNS-2 and Co/N-C. (e) Raman spectra of the Co/N-CNS-2 prepared with different contents of cobalt salts. (f) Nitrogen adsorption/desorption isotherms of the Co/N-CNS-0, Co/N-CNS-1, Co/N-CNS-2, Co/N-CNS-2(700) and Co/N-CNS-2(900).

the Co/N-CNS-2 shows high ORR catalytic performance. CV and linear sweep voltammetry (LSV) are also measured to evaluate their ORR catalytic performance of Co/N-CNS and Pt/C catalysts (figures 4(b) and S8). The Co/N-CNS-2 catalyst shows excellent ORR performance with prominently positive onset potential (E_{onset}, 0.97 V vs. RHE) and high half-wave potential ($E_{1/2}$, 0.855 V vs. RHE), compared with that of Pt/C catalyst (0.98 V and 0.85 V vs. RHE, respectively). The Co/N-CNS-2 shows a diffusion-limiting current density of 4.7 mA cm^{-2}, which is very close to commercial Pt/C of 4.9 mA cm^{-2}, suggesting that the Co/N-CNS-2 shows the potential of substituting to commercial Pt/C. As a contrast, the Co/N-CNS-0, Co/N-CNS-1 and Co/N-C show inferior ORR performance compared with that of Co/N-CNS-2. The dual doping of cobalt and nitrogen endows the as-prepared Co/N-CNS with more active sites (mainly Co-N_x and pyridinic-N). On this basis, the E_{onset} and $E_{1/2}$ of the Co/N-CNS become more positive with decreased VB2/$Co(OAc)_2$ ratio from 40 to 20, but decrease with continually decreased VB2/$Co(OAc)_2$ mass ratio to 10 (figures 4(c) and (d)). This is because excessive cobalt ions among the precursor will form large aggregated cobalt particles during high-temperature pyrolysis, resulting in the damage of porous structures in the Co/N-CNS. Figure 4(e) exhibits that the Co/N-CNS-2 shows optimized ORR catalytic performance among the Co/N-CNS. The Co/N-CNS-2(700) exhibits decreased ORR catalytic activity due to its insufficient pore structures. Similarly, the collapse of pore structures of the Co/N-CNS-2(900) leads to decreased ORR catalytic performance. Low graphitization degree and low conductivity of the Co/N-CNS-2(700) obtained at relatively low pyrolysis temperature will weaken the ORR performance to a certain extent, while higher pyrolysis temperature will lead to large graphitization degree with simultaneous losses of doped nitrogen contents and catalytically active sites.

ORR kinetics of the Co/N-CNS catalysts are investigated by calculations of electron transfer number (n) derived from

Table 1. Comparison of ORR catalytic properties of the Co/N-CNS-2 with heteroatom-doped carbon hybrid materials in the literature.

Samples	Shifts vs. E of Pt/C [mV]		*n*	References
	$E_{1/2}$	E_{onset}		
3D MPC	−25	−5	3.81–3.96	[29]
NPMC-1000	0	−5	4.0	[6]
MZ8-S-P	−16	5	3.5–3.9	[57]
N-CNS-120	0	30	3.9–4.0	[8]
NWCN-7	−69	−70	3.75–3.90	[59]
CPANI-Fe-NaCl	−58	−60	3.8–4.0	[30]
Mn-C-NO	−50	−50	3.89–4.0	[56]
MnO_2/N-HGS	−10	−20	3.65–3.85	[53]
RGO/P/2Co	−25	−16	3.9	[58]
BC	−29	50	3.8	[11]
NGRW	−15	−20	3.95	[54]
Co-N_x-OMMC	−10	−20	3.9	[55]
Co/N-CNS-2	**5**	**−10**	**3.98**	**This work**

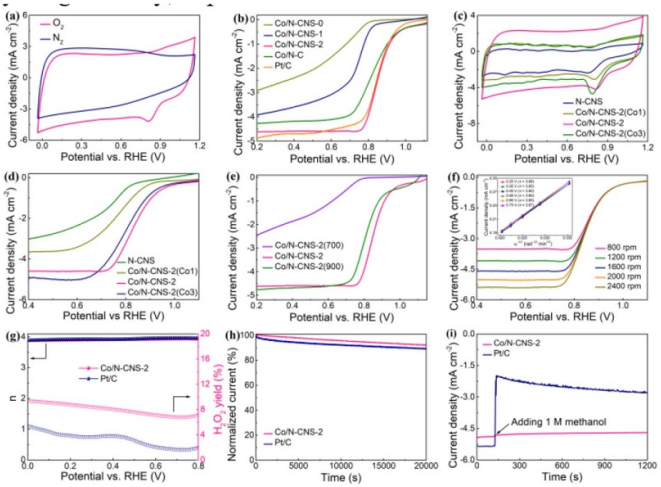

Figure 4. (a) CV curves of the Co/N-CNS-2 in N_2- and O_2-saturated 0.1 M KOH, respectively. (b) LSV curves of the Co/N-CNS-0, Co/N-CNS-1, Co/N-CNS-2, Co/N-C and Pt/C. (c) CV and (d) LSV curves of the Co/N-CNS-2(Co1), Co/N-CNS-2, Co/N-CNS-2(Co3), N-CNS. (e) LSV curves of the Co/N-CNS-2(700), Co/N-CNS-2, Co/N-CNS-2(900). (f) LSV curves of the Co/N-CNS-2 at various rotating speeds. Inset of (f) is K-L plots of the Co/N-CNS-2 at various potentials. (g) H_2O_2 yield and n of the Co/N-CNS-2 and Pt/C from the RRDE curve in O_2-saturated 0.1 M KOH, 1600 rpm. (h) Chronoamperometric responses of the Co/N-CNS-2 and Pt/C in O_2-saturated 0.1 M KOH. (i) Chronoamperometric responses of the Co/N-CNS-2 and Pt/C upon addition of 1 M methanol.

the LSV curves at different rotation speeds (figure 4(f)). Insert of figure 4(f) shows the corresponding Koutechy-Levich (K-L) plots with perfect linearity and parallelism. The Co/N-CNS-2 catalyst shows calculated *n* of 3.98 in potential range of oxygen reduction, indicating its almost four-electron charge transfer process, that equals to commercial Pt/C ($n = 3.98$). Rotating ring disk electrode (RRDE) measurements are also used to calculate the *n* by monitoring the H_2O_2 yields (figure 4(g)). As a result, the Co/N-CNS-2 preferably catalyzed the ORR through a four-electron pathway with the *n* of 3.93, which is close to that of Pt/C (3.98). The H_2O_2 yield of the Co/N-CNS-2 (8.1%) is also approaching to that of Pt/C (5.2%) over the potential range from 0–0.8 V vs. RHE. This result clearly demonstrates the excellent catalytic performance of the Co/N-CNS-2 towards the ORR. The Co/N-CNS-2 with optimized ORR catalytic performance comes from unique 3D honeycombed porous structures with uniform distributions of highly active Co/N_x active sites among carbon skeletons [51, 52]. More importantly, the ORR catalytic properties of the Co/N-CNS-2 exceed most heteroatom-doped carbon catalysts reported in the literature (table 1) [6, 8, 11, 29, 30, 53–59].

Cycling performance and methanol-tolerant durability of the Co/N-CNS-2 and Pt/C catalysts in 0.1 M KOH are compared by conducting chronoamperometry measurements to address their practical applications. High retention of the Co/N-CNS-2 (92%) after continuous testing at 20 000 s indicates its excellent cycling stability compared with that of Pt/C (figure 4(h)). The Pt/C catalyst shows dramatically decreased cathodic current when 1 M methanol is added, whereas the chronoamperometry curve of the Co/N-CNS-2 almost does not decay under the same condition (figure 4(i)), indicating that the Co/N-CNS-2 shows almost no methanol crossover effect. These results clearly show that the Co/N-CNS-2 catalyst exhibits excellent ORR catalytic activity and cycling stability, superior to commercial Pt/C.

A primary Zn-air battery is assembled using carbon cloth-loaded Co/N-CNS-2, Zn plate and Celgard 2332 membrane as cathode, anode and separator, respectively, to further demonstrate the practical applications of the Co/N-CNS-2 catalyst. The electrolyte is a 6 M KOH solution containing 0.2 M zinc acetate. Figure 5(a) indicates that the Co/N-CNS-2-based Zn-air battery works smoothly with an open-circuit potential of 1.54 V, which is higher than that of Pt/C-based Zn-air battery battery (1.49 V). The power densities of Zn-air battery are calculated from the corresponding polarization curves measured at different discharge current densities (figure 5(b)). The open circuit voltage of Zn-air battery with the Co/N-CNS-2 cathode reaches 1.46 V, which is very close to that of Zn-air battery with Pt/C cathode. The highest power density for the Zn-air battery with the Co/N-CNS-2 cathode reaches 138 mW cm^{-2} at the current density of 204 mA cm^{-2}, which is significantly higher than that of Zn-air battery using the Pt/C cathode. The results indicate that the Co/N-CNS-2 catalyst is a very promising alternative to commercial Pt/C as cathode materials for Zn-air battery, which is ascribing to its superior electrocatalytic performance and long-term durability for the ORR. When normalized to the mass of consumed Zn during the discharge process, the specific capacity of our battery is up to 745 mA h $g_{Zn}{}^{-1}$ at the current density of 20 mA cm^{-2}, which is higher than that of battery using Pt/C cathode (figure 5(c)). The operating potential of Zn-air battery using the Co/N-CNS-2 cathode at the current density of 20 mA cm^{-2} (1.18 V) is similar to that of Zn-air battery using the Pt/C cathode. Furthermore, compared with Pt/C, a small potential

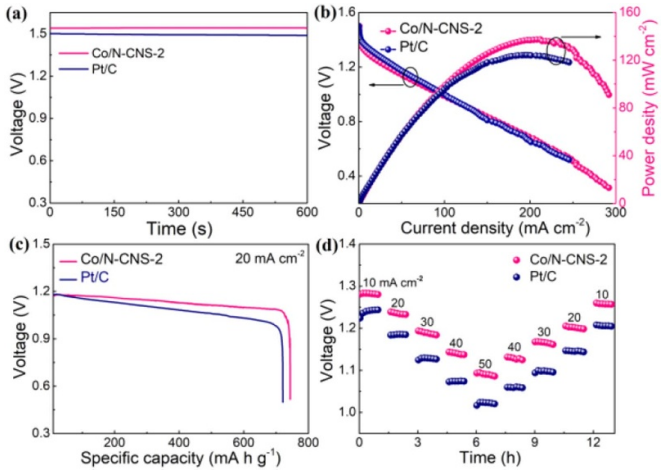

Figure 5. (a) Open circuit voltage curves of as-fabricated Zn-air battery with the Co/N-CNS-2 and Pt/C cathodes, respectively. (b) Polarization curves and power densities of the Co/N-CNS-2 and Pt/C cathodes, respectively. (c) Galvanostatic discharge curves of the Co/N-CNS-2 and Pt/C cathodes at a discharge current density of 20 mA cm^{-2}, respectively. (d) Rate capability of the Co/N-CNS-2 and Pt/C cathodes at different current densities.

drop is observed at the galvanostatic discharge current density of 20 mA cm^{-2}, indicating a stable catalytic stability of the Co/N-CNS-2 catalyst towards the ORR. Figure 5(d) shows that the rate performance of Zn-air battery using the Co/N-CNS-2 cathode is better than that of Zn-air battery using Pt/C cathode. The exceptional rate capability of the Co/N-CNS-2 cathode is ascribing to significantly improved electron transport and ion diffusion pathways among the Co/N-CNS-2.

4. Conclusion

In summary, a hypersaline-protected pyrolysis strategy is developed for the preparation of cobalt and nitrogen co-doped carbon nanosheet (Co/N-CNS). The NaCl salts not only act as a recyclable template boosting the formation of a 3D honeycombed structure among the Co/N-CNS, but also act as an encapsulated pyrolysis media for largely improving the carbonization yield and N-doping efficiency. Due to 3D honeycombed pore structures with highly efficient ion/charge/oxygen transports, the Co/N-CNS catalyst exhibits a highly active ORR activity ($E_{1/2}$ at 0.855 V vs. RHE) and remarkable cycling stability (a retention above 92% after 20 000 s) in 0.1 M KOH electrolyte. As a demonstration, a Zn-air battery using the Co/N-CNS cathode demonstrates a high power density of 138 mW cm^{-2} at 204 mA cm^{-2}, high specific capacity and operating voltage up to 745 mA h $g_{Zn}{}^{-1}$ and 1.18 V, respectively, at 20 mA cm^{-2}. Furthermore, the hypersaline-protected pyrolysis strategy is easily extended to develop various metal/nitrogen co-doped porous carbon electrocatalysts with a competitive ORR catalytic performance towards next-generation ORR-involved energy conversion processes.

Acknowledgments

This work was supported by the National Natural Science Foundation of China (51773035), the Natural Science Foundation of Shanghai (17ZR1439900), and the Shanghai Scientific and Technological Innovation Project (18JC1410600).

ORCID iD

Chao Zhang https://orcid.org/0000-0003-1255-7183

References

[1] Shao M, Chang Q, Dodelet J P and Chenitz R 2016 Recent advances in electrocatalysts for oxygen reduction reaction *Chem. Rev.* **116** 3594–657
[2] Nie Y, Li L and Wei Z 2015 Recent advancements in Pt and Pt-free catalysts for oxygen reduction reaction *Chem. Soc. Rev.* **44** 2168–201
[3] Tovini M F, Patil B, Koz C, Uyar T and Yılmaz E 2018 Nanohybrid structured RuO2/Mn2O3/CNF as a catalyst for Na–O2 batteries *Nanotechnology* **29** 475401
[4] Li S, Cui Z, Li D, Yue G, Liu J, Ding H, Gao S, Zhao Y, Wang N and Zhao Y 2019 Hierarchically structured electrospinning nanofibers for catalysis and energy storage *Compos. Commun.* **13** 1–11
[5] Guo H, Zhou J, Li Q, Li Y, Zong W, Zhu J, Xu J, Zhang C and Liu T 2020 Emerging dual-channel transition-metal-oxide quasiaerogels by self-embedded templating *Adv. Funct. Mater.* **30** 2000024
[6] Zhang J, Zhao Z, Xia Z and Dai L 2015 A metal-free bifunctional electrocatalyst for oxygen reduction and oxygen evolution reactions *Nat. Nanotechnol.* **10** 444
[7] Zhang C, Antonietti M and Fellinger T-P 2014 Blood Ties: Co3o4 decorated blood derived carbon as a superior bifunctional electrocatalyst *Adv. Funct. Mater.* **24** 7655–65
[8] Yu H, Shang L, Bian T, Shi R, Waterhouse G I N, Zhao Y, Zhou C, Wu L-Z, Tung C-H and Zhang T 2016 Nitrogen-doped porous carbon nanosheets templated from g-C3N4 as metal-free electrocatalysts for efficient oxygen reduction reaction *Adv. Mater.* **28** 5080–6
[9] Du C *et al* 2019 Balancing the micro-mesoporosity for activity maximization of N-doped carbonaceous electrocatalysts for the oxygen reduction reaction *ChemSusChem* **12** 1017–25
[10] Zhang C, Hou L, Cheng C, Zhuang Z, Zheng F and Chen W 2018 Nitrogen and phosphorus Co-doped hollow carbon spheres as efficient metal-free electrocatalysts for the oxygen reduction reaction *ChemElectroChem* **5** 1891–8
[11] Gong X, Liu S, Ouyang C, Strasser P and Yang R 2015 Nitrogen- and phosphorus-doped biocarbon with enhanced electrocatalytic activity for oxygen reduction *ACS Catal.* **5** 920–7
[12] Zhou J, Wang Y and Zhang C 2019 Synthesis and electrochemical performance of core-shell NiCo2S4@nitrogen, sulfur dual-doped carbon composites via confined sulfidation strategy in a polydopamine nanoreactor *Compos. Commun.* **12** 74–79
[13] Xiao C, Chen X and Tang Y 2017 Surface-rough Fe-N/C composite wrapped on carbon nanotubes as efficient electrocatalyst for oxygen reduction reaction *Nanotechnology* **28** 225401
[14] Guo H, Feng Q, Zhu J, Xu J, Li Q, Liu S, Xu K, Zhang C and Liu T 2019 Cobalt nanoparticle-embedded nitrogen-doped carbon/carbon nanotube frameworks derived from a metal–organic framework for tri-functional ORR, OER and HER electrocatalysis *J. Mater. Chem. A* **7** 3664–72

[15] Shang L, Yu H, Huang X, Bian T, Shi R, Zhao Y, Waterhouse G I N, Wu L-Z, Tung C-H and Zhang T 2016 Well-dispersed ZIF-derived Co,N-Co-doped carbon nanoframes through mesoporous-silica-protected calcination as efficient oxygen reduction electrocatalysts *Adv. Mater.* **28** 1668–74

[16] Xiang D, Bo X, Gao X, Du C, Li P, Zhu L and Chen W 2019 Bimetal- and nitrogen-codoped spherical porous carbon with efficient catalytic performance towards oxygen reduction reaction in alkaline media *J. Colloid Interface Sci.* **534** 655–64

[17] Zhang Z, Yang S, Li H, Zan Y, Li X, Zhu Y, Dou M and Wang F 2019 Sustainable carbonaceous materials derived from biomass as metal-free electrocatalysts *Adv. Mater.* **31** 1805718

[18] Liu M, Yang Z, Sun H, Lai C, Zhao X, Peng H and Liu T 2016 A hybrid carbon aerogel with both aligned and interconnected pores as interlayer for high-performance lithium–sulfur batteries *Nano Res.* **9** 3735–46

[19] Huang K, Zhang W, Li J, Fan Y, Yang B, Rong C, Qi J, Chen W and Yang J 2020 *In situ* anchoring of zeolite imidazole framework-derived Co, N-doped porous carbon on multiwalled carbon Nanotubes toward efficient electrocatalytic oxygen reduction *ACS Sustain. Chem. Eng.* **8** 478–85

[20] Zhang R, Zhang C and Chen W 2016 FeP embedded in N, P dual-doped porous carbon nanosheets: an efficient and durable bifunctional catalyst for oxygen reduction and evolution reactions *J. Mater. Chem. A* **4** 18723–9

[21] Kaur P, Verma G and Sekhon S S 2019 Biomass derived hierarchical porous carbon materials as oxygen reduction reaction electrocatalysts in fuel cells *Prog. Mater Sci.* **102** 1–71

[22] Huang Y, Wang Y, Tang C, Wang J, Zhang Q, Wang Y and Zhang J 2019 Atomic modulation and structure design of carbons for bifunctional electrocatalysis in metal-air batteries *Adv. Mater.* **31** 1803800

[23] Huang S, Li Y, Feng Y, An H, Long P, Qin C and Feng W 2015 Nitrogen and fluorine co-doped graphene as a high-performance anode material for lithium-ion batteries *J. Mater. Chem. A* **3** 23095–105

[24] Liu Y, Yan Y, Li K, Yu Y, Wang Q and Liu M 2019 A high-areal-capacity lithium–sulfur cathode achieved by a boron-doped carbon–sulfur aerogel with consecutive core–shell structures *Chem. Commun.* **55** 1084–7

[25] Zhang R, He S, Lu Y and Chen W 2015 Fe, Co, N-functionalized carbon nanotubes *in situ* grown on 3D porous N-doped carbon foams as a noble metal-free catalyst for oxygen reduction *J. Mater. Chem. A* **3** 3559–67

[26] Tang J, Liu J, Li C, Li Y, Tade M O, Dai S and Yamauchi Y 2015 Synthesis of nitrogen-doped mesoporous carbon spheres with extra-large pores through assembly of diblock copolymer micelles *Angew. Chem. Int. Ed.* **54** 588–93

[27] Chen S, Bi J, Zhao Y, Yang L, Zhang C, Ma Y, Wu Q, Wang X and Hu Z 2012 Nitrogen-doped carbon nanocages as efficient metal-free electrocatalysts for oxygen reduction reaction *Adv. Mater.* **24** 5593–7

[28] Liu S, Xu J, Zhu J, Chang Y, Wang H, Liu Z, Xu Y, Zhang C and Liu T 2017 Leaf-inspired interwoven carbon nanosheet/nanotube homostructures for supercapacitors with high energy and power densities *J. Mater. Chem. A* **5** 19997–20004

[29] Wang W, Chen W, Miao P, Luo J, Wei Z and Chen S 2017 NaCl crystallites as dual-functional and water-removable templates to synthesize a three-dimensional graphene-like macroporous Fe-N-C catalyst *ACS Catal.* **7** 6144–9

[30] Ding W, Li L, Xiong K, Wang Y, Li W, Nie Y, Chen S, Qi X and Wei Z 2015 Shape fixing via salt recrystallization: a morphology-controlled approach to convert nanostructured polymer to carbon nanomaterial as a highly active catalyst for oxygen reduction reaction *J. Am. Chem. Soc.* **137** 5414–20

[31] Lai L, Potts J R, Zhan D, Wang L, Poh C K, Tang C, Gong H, Shen Z, Lin J and Ruoff R S 2012 Exploration of the active center structure of nitrogen-doped graphene-based catalysts for oxygen reduction reaction *Energy Environ. Sci.* **5** 7936–42

[32] Niwa H *et al* 2011 X-ray photoemission spectroscopy analysis of N-containing carbon-based cathode catalysts for polymer electrolyte fuel cells *J. Power Sources* **196** 1006–11

[33] Cheng Q P, Zhao N, Lyu S S, Tian Y, Gao F, Dong L, Jiang Z, Zhang J, Tsubaki N and Li X G 2019 Tuning interaction between cobalt catalysts and nitrogen dopants in carbon nanospheres to promote Fischer-Tropsch synthesis *Appl. Catal.* B **248** 73–83

[34] Wohlgemuth S-A, White R J, Willinger M-G, Titirici -M-M and Antonietti M 2012 A one-pot hydrothermal synthesis of sulfur and nitrogen doped carbon aerogels with enhanced electrocatalytic activity in the oxygen reduction reaction *Green Chem.* **14** 1515–23

[35] Wang Y, Wang K, Zhang C, Zhu J, Xu J and Liu T 2019 Solvent-exchange strategy toward aqueous dispersible MoS2 nanosheets and their nitrogen-rich carbon sphere nanocomposites for efficient lithium/sodium ion storage *Small* **15** e1903816

[36] Wang X-R, Liu J-Y, Liu Z-W, Wang W-C, Luo J, Han X-P, Du X-W, Qiao S-Z and Yang J 2018 Identifying the key role of pyridinic-N–Co bonding in synergistic electrocatalysis for reversible ORR/OER *Adv. Mater.* **30** 1800005

[37] Tian X, Luo J, Nan H, Fu Z, Zeng J and Liao S 2015 Binary transition metal nitrides with enhanced activity and durability for the oxygen reduction reaction *J. Mater. Chem. A* **3** 16801–9

[38] Zhang W, Yao X, Zhou S, Li X, Li L, Yu Z and Gu L 2018 ZIF-8/ZIF-67-derived Co-Nx-embedded 1D porous carbon nanofibers with graphitic carbon-encased Co nanoparticles as an efficient bifunctional electrocatalyst *Small* **14** 1800423

[39] Wu C, Zhang Y, Dong D, Xie H and Li J 2017 Co9S8 nanoparticles anchored on nitrogen and sulfur dual-doped carbon nanosheets as highly efficient bifunctional electrocatalyst for oxygen evolution and reduction reactions *Nanoscale* **9** 12432–40

[40] Guo H, Feng Q, Xu K, Xu J, Zhu J, Zhang C and Liu T 2019 Self-templated conversion of metallogel into heterostructured TMP@carbon quasiaerogels boosting bifunctional electrocatalysis *Adv. Funct. Mater.* **29** 1903660

[41] Wang Q, Shang L, Shi R, Zhang X, Zhao Y, Waterhouse G I N, Wu L-Z, Tung C-H and Zhang T 2017 NiFe layered double hydroxide nanoparticles on Co,N-codoped carbon nanoframes as efficient bifunctional catalysts for rechargeable zinc–air batteries *Adv. Energy Mater.* **7** 1700467

[42] Guo C, Liao W, Li Z and Chen C 2015 Exploration of the catalytically active site structures of animal biomass-modified on cheap carbon nanospheres for oxygen reduction reaction with high activity, stability and methanol-tolerant performance in alkaline medium *Carbon* **85** 279–88

[43] Wang J-Y, Ouyang T, Li N, Ma T and Liu Z-Q 2018 S, N co-doped carbon nanotube-encapsulated core-shelled CoS2@Co nanoparticles: efficient and stable bifunctional catalysts for overall water splitting *Sci. Bull.* **63** 1130–40

[44] Chen S, Cheng J, Ma L, Zhou S, Xu X, Zhi C, Zhang W, Zhi L and Zapien J A 2018 Light-weight 3D Co–N-doped hollow carbon spheres as efficient electrocatalysts for rechargeable zinc–air batteries *Nanoscale* **10** 10412–9

[45] Yan Y *et al* 2019 Hydrogel self-templated synthesis of Na3V2(PO4)3@C@CNT porous network as ultrastable

cathode for sodium-ion batteries *Compos. Commun.* **13** 97–102
[46] Zhang W, Sherrell P, Minett A I, Razal J M and Chen J 2010 Carbon nanotube architectures as catalyst supports for proton exchange membrane fuel cells *Energy Environ. Sci.* **3** 1286–93
[47] Chen Y, Li Y, Yao F, Peng C, Cao C, Feng Y and Feng W 2019 Nitrogen and fluorine co-doped holey graphene hydrogel as a binder-free electrode material for flexible solid-state supercapacitors *Sustain. Energ. Fuels* **3** 2237–45
[48] Li L, Zhang Y, Lu H, Wang Y, Xu J, Zhu J, Zhang C and Liu T 2020 Cryopolymerization enables anisotropic polyaniline hybrid hydrogels with superelasticity and highly deformation-tolerant electrochemical energy storage *Nat. Commun.* **11** 62
[49] Wang Q, Miao H, Sun S, Xue Y and Liu Z 2018 One-pot synthesis of Co3 O4/Ag nanoparticles supported on N-doped graphene as efficient bifunctional oxygen catalysts for flexible rechargeable zinc-air batteries *Chem. Eur. J.* **24** 14816–23
[50] Zhang K, Zhang Y, Zhang Q, Liang Z, Gu L, Guo W, Zhu B, Guo S and Zou R 2020 Metal-organic framework-derived Fe/Cu-substituted Co nanoparticles embedded in CNTs-grafted carbon polyhedron for Zn-air batteries *Carbon Energy* (https://doi.org/10.1002/cey2.35)
[51] Jiang H, Gu J X, Zheng X S, Liu M, Qiu X Q, Wang L B, Li W Z, Chen Z F, Ji X B and Li J 2019 Defect-rich and ultrathin N doped carbon nanosheets as advanced trifunctional metal-free electrocatalysts for the ORR, OER and HER *Energy Environ. Sci.* **12** 322–33
[52] Chai G S, Shin I S and Yu J-S 2004 Synthesis of ordered, uniform, macroporous carbons with mesoporous walls templated by aggregates of polystyrene spheres and silica particles for use as catalyst supports in direct methanol fuel cells *Adv. Mater.* **16** 2057–61
[53] Yu Q, Xu J, Wu C, Zhang J and Guan L 2016 MnO2 nanofilms on nitrogen-doped hollow graphene spheres as a high-performance electrocatalyst for oxygen reduction reaction *ACS Appl. Mater. Interfaces* **8** 35264–9
[54] Yang H B *et al* 2016 Identification of catalytic sites for oxygen reduction and oxygen evolution in N-doped graphene materials: development of highly efficient metal-free bifunctional electrocatalyst *Sci. Adv.* **2** 1501122
[55] Sun T, Xu L, Li S, Chai W, Huang Y, Yan Y and Chen J 2016 Cobalt-nitrogen-doped ordered macro-/mesoporous carbon for highly efficient oxygen reduction reaction *Appl. Catal. B* **193** 1–8
[56] Qu K, Zheng Y, Dai S and Qiao S Z 2016 Graphene oxide-polydopamine derived N, S-codoped carbon nanosheets as superior bifunctional electrocatalysts for oxygen reduction and evolution *Nano Energy* **19** 373–81
[57] Qian Y, An T, Birgersson K E, Liu Z and Zhao D 2018 Web-like interconnected carbon networks from NaCl-assisted pyrolysis of ZIF-8 for highly efficient oxygen reduction catalysis *Small* **14** 1704169
[58] He T *et al* 2017 *In situ* fabrication of defective conx single clusters on reduced graphene oxide sheets with excellent electrocatalytic activity for oxygen reduction *ACS Appl. Mater. Interfaces* **9** 22490–501
[59] Gu D, Wang F, Yan K, Ma R and Wang J 2018 A thermally decomposable template route to synthesize nitrogen-doped wrinkled carbon nanosheets as highly efficient and stable electrocatalysts for the oxygen reduction reaction *ACS Sustain. Chem. Eng.* **6** 1951–60